Nature Communications

https://doi.org/10.1038/s41467-025-67936-6

Article in Press

Magnetically actuated momentum-driven millirobots

Received: 11 September 2024

Accepted: 12 December 2025

Cite this article as: Wang, M., Wu, W., Zheng, Z. *et al.* Magnetically actuated momentum-driven millirobots. *Nat Commun* (2025). https://doi.org/10.1038/s41467-025-67936-6

Min Wang, Wenlong Wu, Zeju Zheng, Wei Dai, Tianyi Wu, Rui Liu, Yuxuan Xiang, Steven Wang, Jiachen Zhang, Zuankai Wang & Jun Liu

Magnetically Actuated Momentum-Driven Millirobots

Author Information

Min Wang[1,2,3], Wenlong Wu[3,4], Zeju Zheng[3,5], Wei Dai[3], Tianyi Wu[3], Rui Liu[3], Yuxuan Xiang[6], Steven Wang[3], Jiachen Zhang[6*], Zuankai Wang[7*], Jun Liu[1,3*]

[1] **Department of Data and Systems Engineering, The University of Hong Kong, Hong Kong SAR, China**

[2] **School of Mechanical and Electrical Engineering, Central South University, Changsha, China**

[3] **Department of Mechanical Engineering, City University of Hong Kong, Hong Kong SAR, China**

[4] **Academy of Electronic Science and Technology of CETC, Beijing, China**

[5] **Thrust of Sustainable Energy and Environment, Hong Kong University of Science and Technology (Guangzhou), Guangzhou, China**

[6] **Department of Biomedical Engineering, City University of Hong Kong, Hong Kong SAR, China**

[7] **Department of Mechanical Engineering, The Hong Kong Polytechnic University, Hong Kong SAR, China**

Corresponding author

* To whom correspondence should be addressed:

jzhang.bme@cityu.edu.hk, zk.wang@polyu.edu.hk, djliu@hku.hk

Abstract

Designing millirobots capable of navigating high-friction environments remains a significant challenge due to limitations in force output and the absence of efficient transmission mechanisms at small scales. In this study, we introduce a magnetically inner actuated millirobot capable of generating a thrust force exceeding 15 N with a body weight of 5.82 g for moving across diverse frictional terrains. The inner-actuated millirobot features a dual-coil array positioned at either end of a plastic skeleton and a permanent magnet accommodated in the center channel of the skeleton. When powered by a 0.5 A current, the internal magnetic interaction propels the magnet to a velocity of 2.10 m/s within 17 ms, striking the body wall to produce a powerful instantaneous thrust that overcomes friction forces. Experimental results demonstrate the millirobot's ability to operate in viscous oil, traverse sand and granular media, and transport cargo exceeding 300 times its body weight. Furthermore, the magnetically inner actuated millirobot shows promising potential for accessing confined tubular environments. This magnetically inner-actuated design, leveraging momentum conservation for propulsion, enables millirobots with high force capacity for high-friction and confined-space applications.

Introduction

Millirobots exhibit remarkable capabilities in navigating challenging and hazardous environments, such as subterranean spaces, disaster sites, and tubular structures. Recent advances in miniature robotics have enabled a range of applications, including wall-climbing[1, 2, 3], pipeline inspection[4], drug delivery[5, 6], deep-sea inspection[7] and cargo transportation[8,9]. However, due to the scaling effect, current millirobots face limitations in force and energy output at small scales (e.g., less than 10 cm in length and 10 g in mass), which constrains their broad applicability. Developing a millirobot capable of generating sufficient force and energy remains challenging but is crucial for expanding their use in high-friction environments and confined spaces[10].

Various efforts have been made to improve the load-bearing capacity of millirobots[11,12]. For example, hydraulically amplified self-healing electrostatic actuators have demonstrated the ability to lift over 200 times their weight[13]. Additionally, 3D-printed pneumatic actuators have demonstrated the ability to lift cargo weighting more than hundreds of times their own body weight[14]. Moreover, reconfigurable modular robots have been built by attaching magnetic units to a plastic robot frame to deliver the cargo of various shapes[15]. However, achieving effective locomotion with a high load-to-weight ratio remains unsolved due to significant friction forces. Although several millirobots demonstrated impressive cargo delivery capabilities on the ground[16, 17], most actuation mechanisms restrict their movement to wide, flat terrains and fail to adapt to high-resistance environments, particularly when robots are tested in confined spaces like granular medium and collapsed tubular structures.

High-friction environments, such as viscous oil, subterranean mediums, and rough ground, are challenging for millirobotic navigation. Several actuation mechanisms have been proposed to address these challenges. For example, flagella-inspired millirobots have demonstrated locomotion in viscous environments[18]. The explosion and jumping actuation in granular media were demonstrated using a magnetic phase-change actuator[19]. Additionally, pneumatic-driven expanding robots have been designed for operation in granular environments[20]. These studies succeeded in overcoming high friction forces in specific environments. However, a universal design and actuation mechanism capable of generating sufficient force for traveling through diverse high-friction terrains remains undeveloped.

To enhance the thrust force of magnetic systems, propulsion mechanisms based on the principle of momentum conservation have proven to be effective. Typically, magnetic robots driven by the magnetic field gradients are limited in their ability to achieve high force output for tissue penetration. To address this limitation, researchers have developed a magnetic hammer actuation system, which employs an MRI system to accelerate a magnet, generating large impulse forces upon impact with the robot frame[21]. Similarly, a pulse-actuated collision robot has been introduced to overcome the force limitations of magnetic robotic surgery, and this robot has been demonstrated in biological tissue suturing applications[10]. After that, researchers developed a triple-magnet system to improve the thrust force. By adjusting the

orientation of the external magnet, the Newton-level forces through the attraction between embedded magnets were achieved for potential applications in tissue biopsy[22]. While the pulse impact mechanism has significantly improved actuation force, these systems remain limited by their small working range due to reliance on a fixed external magnetic source. They also suffer from high power consumption, as the magnetic actuation force decreases inversely with the fourth power of the distance between the robot and the magnetic source[23].

To address the aforementioned limitations, we propose a magnetically inner actuated millirobot (MiaBot) with integrated actuation coils and a magnet. As depicted in Fig. 1A, the millirobot consists of an inner permanent magnet, a tube frame to accommodate the magnet, two stoppers to limit the stroke, and two electromagnetic coils positioned at either end with opposite winding directions. To build the MiaBot, the plastic frame with a central channel is first made of polyetheretherketone (PEEK) by 3D printing and polishing to minimize the friction of the inner surface. Then, the electromagnetic coils are constructed by winding 200 turns of copper wire with a total resistance of 12.4 Ω. A cylindrical NdFeB magnet (N52, 6.35 mm in diameter and length, from K&J Ltd.) is embedded within the center channel for inner actuation. After that, two stoppers are attached to the two ends of the robot frame using super glue. The resulting MiaBot is lightweight (5.82 g) and compact (Ø 12 mm × 32 mm). The Detailed design principles, assembly process and dimensions of components are summarized in Fig. S1.

When the MiaBot is driven by a square wave ranging from 0.5 A to -0.05A. Fig. 1C depicts the snapshots of the inner magnet and MiaBot during one cycle actuation. During propulsion, the magnet traverses the central channel in 14 ms, generating a strong impact force that propels the MiaBot forward. For the reposition process, the impact force is insufficient to overcome static friction, preventing backward displacement. Fig. 1D demonstrates that the magnet can pass through the center channel of the robot frame within 20 ms, causing a theoretical thrust of up to 19.01 N. By leveraging local magnetic field actuation and momentum conservation, the robot overcomes substantial environmental resistance to perform challenging tasks, including navigation through granular media, operation in high-viscosity silicone oil, and cargo transport exceeding 300 times its weight (Fig. 1E). Fig. 1B compares MiaBot's load-carrying

capability with that of state-of-the-art millirobots (weighing less than 10 grams) using various actuation mechanisms, including shape memory alloy[24, 25, 26], dielectric elastomer actuators[27, 28, 29, 30], piezoelectric actuators[31, 32, 33, 34], magnetic robots[17, 35, 36, 37, 38, 39], and photothermal actuators[40, 41, 42, 43]. Moreover, we also compare the loading performance with natural creatures like insects and mammals (data in Tables S2 and S3). The results show that MiaBot outperforms most miniature robots and surpasses the majority of natural creatures, falling short only of beetles.

In summary, MiaBot, which utilizes local magnetic field actuation and a momentum conservation-based propulsion mechanism, offers three advantages: (1) Lightweight and compact design: The simple energy conversion mechanism eliminates the need for complex transmission components such as gears and bearings. (2) Unrestricted workspace: By integrating electromagnetic coils and a magnet, MiaBot operates with a self-contained actuation system without relying on external magnetic sources that confines the workspace. (3) High force and payload capacity: The rapid movement of the internal magnet generates a powerful inertial impact, enabling operation in high-friction environments. Overall, MiaBot advances the design of next-generation millirobots with a large force output for applications in high-friction environments and confined spaces.

Results

Robot actuation mechanism and kinematic characterization

The actuation coils are placed symmetrically at each end of the millirobot frame and are wound in opposite directions. This configuration allows the same magnetic pole (either north or south) to face inward when supplied with the same current, resulting in the same actuation force on the magnet by the left and right coils (e.g., left repulsion/right attraction or left attraction/right repulsion, as shown in Fig. 1D). When an electric current is applied to the electromagnetic coils, the theoretical magnetic force on the inner magnet at any given position along the center axis is calculated by

$$\boldsymbol{F_z} = \nabla(\boldsymbol{m} \cdot \boldsymbol{B_z}) \tag{1}$$

where $\boldsymbol{m}$ represents the magnetic moment of the sliding magnet. The calibration of $\boldsymbol{m}$ is shown in Fig. S2. $\boldsymbol{B_z}$ is the overall magnetic field generated by two coils. The overall magnetic field generated by the left coil set and right coil set can be expressed as

$$B_z = \frac{\mu_0 n_l n_t}{2L_w(R_2 - R_1)} I \int_0^{L_w} \int_{R_1}^{R_2} \left(\frac{R^2}{((z-l)^2 + R^2)^{1.5}} - \frac{R^2}{((L_c - L_w + l - z)^2 + R^2)^{1.5}} \right) dRdl \qquad (2)$$

where μ_0 is the vacuum permeability, n_l is the coil's turns of each layer, n_t is the layer number of the coil, I is the input current, R_1 and R_2 are the inner and outer radius of the coil, z is the distance from the calculated point to the end of the coil, L_C is the length of the center channel, L_w is the width of a coil set R is the radius of the integral coil and l represents the distance from the end of the coil to the center of the integral coil loop. A detailed distribution of the magnetic field generated by the coils is shown in Fig. S3, and the calculated interaction force between the coils and the magnet can be referred to Fig. S4.

To sustain continuous locomotion, the MiaBot is actuated using a square wave with a bias current as the input signal. The polarity with a larger amplitude (denoted as I_l) is used to actuate the inner magnet, serving as the primary contributor to MiaBot's locomotion. Meanwhile, the opposite polarity with a smaller amplitude (denoted as I_s) repositions the magnet, ensuring periodic and continuous movement. The resulting actuation force by I_s is carefully controlled to reposition the inner magnet while minimizing the impact force to remain below the static friction force to avoid unwanted cancellation of the positive movement. Accordingly, I_s is set to -0.05 A in this paper unless otherwise stated in the following experiments. This paper focuses on investigating the effect of I_l and input frequency on MiaBot's locomotion, as they are the primary factors influencing robot displacement.

The MiaBot is observed to have two distinct locomotion modes as the load increases with the input current. As illustrated in Fig. 2A, when MiaBot carries no load, the attraction force between the magnet and the coils dominates its locomotion. The reason is that the static friction between the robot frame and the ground is insufficient to counteract the attraction force, causing the magnet and the frame to move toward each other. Conversely, when carrying a heavy load, the inertial impact force of the magnet becomes the primary factor on the robot's locomotion, resulting in a consistent movement direction for both the inner magnet

and the robot frame. Additionally, a critical region emerges where locomotion exhibits directional instability as environmental resistance approaches the magnetic actuation force. Within this region, the system oscillatory motion or unsteady swaying rather than stable unidirectional movement. Fig. S5 provides signal selection guidelines to avoid this unstable operational zone across varying environments. Then, we test input currents I_l ranging from 0.1 A to 0.5 A and loads from 0 g to 100 g, as illustrated in Fig. 2B. The results indicate that the attraction-dominated region occurs only when the load is below 40 g. The MiaBot offers distinct advantages in these two modes. When the attraction force dominates, the MiaBot achieves large displacement and high speed. In contrast, when the inertial force dominates, the robot generates a significant instantaneous output force, enabling MiaBot to operate in high-frictional environments (The locomotion process of this locomotion mode is shown in Fig. S6).

To study the kinematics and increase the actuation power, we develop a theoretical model to optimize the design parameters of center channel length (L_c) and the wideness of the actuation coil set (L_w) simultaneously. A longer L_c can increase the magnet's acceleration time, resulting in a more significant impacting force. However, if the channel length is excessively long, the pair of coils are separated too far apart, leading to a diminished magnetic gradient for driving the inner magnet. A narrow yet thick coil set yields a strong magnetic field nearby, but the magnetic field strength decreases in the near central region. In contrast, wide and flat coils enhance the magnetic density near the central area while reducing the density near the coil. Given a constant input of 1.0 A, Fig. 2C explores the effect of L_c ranging from 20 mm to 35 mm, and L_w ranging from 3 mm to 8 mm on the inertial impact speed of the magnet. The optimal configuration yields an impressive impact velocity of the magnet at 3.11 m/s. As expected, the impact speed demonstrates an increased trend with the length of the channel. However, this rate of increase gradually diminishes once the length reaches 30 mm, with only a marginal 0.36% increase observed between 30 mm and 35 mm. Based on these results, and to simplify the design, a coil width of 5 mm and a channel length of 30 mm were selected as the design parameters for the MiaBot in the following work.

To validate the simulation results, we experimentally measured the travel time of the inner magnet with varied coil set widths and input currents ranging from 0.1 A to 1.0 A. As shown in Fig. 2D, the experimental

results align with the simulation and confirm that the robot with a 5 mm coil set propels the magnet faster than those with 3 mm and 8 mm wide coils. Moreover, the results indicate that the magnet can pass the center channel in a short time. Specifically, with an input current of 0.1 A, the inner magnet traverses the center channel in less than 50 ms, while at 1.0 A, the time reduces to under 15 ms. We also observed that only minor fluctuations occurred when the coil width varied between 4 mm and 6 mm (Fig. S7), indicating that manual coil set wiring is a viable fabrication method for the MiaBot. Subsequently, we calculated the velocity of the inner magnet before impacting under the input currents ranging from 0.1 A to 1.0 A (Fig. 2E). The results show that the inner magnet passes through the center channel at high speed. Specifically, the theoretical impact speed increases from 0.98 m/s to 3.10 m/s as the input current is increased from 0.1 A to 1.0 A. The measured results indicate that the magnet takes longer to traverse the channel and impacts at a lower speed (0.98 m/s and 2.93 m/s by 0.1 A and 1.0 A excitation, respectively) than predicted by the simulation. This discrepancy among experimental measurements can be attributed to the neglect of friction between the inner magnet and the frame in the simulation and the idealized assumption of perfect alignment between the magnet's axis and the coil axis. With the optimized design parameters, the velocity of the unloaded MiaBot was measured at frequencies from 1 Hz to 15 Hz (with I_l=0.5 A) as depicted in Fig. 2F. The results demonstrate that MiaBot can reach a maximum speed of 113.66 mm/s, equal to 3.55 body length per second, at a frequency of 9 Hz.

In addition to the current input and the design parameters of the robot frame, the size of the magnet significantly influences the dynamic performance of MiaBot. The scalability of the magnet in terms of diameter and length is examined in Fig. S8. This analysis assumes a consistent gap between the magnet and the frame and a consistent traveling distance of the magnet. The results indicate that an increase in diameter leads to a decrease in impact velocity but an increase in impact energy. However, the impact energy initially increases and then decreases with the length of the magnet because a longer central channel always comes along with a smaller magnetic field gradient. Additionally, MiaBot's efficiency decreases as the input current increases. At the efficiency is 10.41% when the input current is 0.1 A, which declines to 6.32% as the input current increased to 0.5 A. The thermal effects and actuation efficiency of MiaBot are presented

in Fig. S9. Following 300 seconds of actuation, the temperature rises by less than 5°C with an input current of 0.1 A, while reaching 48°C at 0.5 A. This temperature regime neither damages the robot's frame material nor alters the permanent magnets' magnetic properties. However, to ensure the thermal stability of the enamel insulation on the copper winding, continuous operation exceeding 300 seconds is not recommended, as prolonged thermal loading may degrade the insulation's performance and compromise winding reliability. As a result, the 0.5 A was selected as the input current (I_l) in the following experiments unless otherwise stated.

Inertial impact force and loading performance

To quantify the powerful inertial impact force, a high-frequency force sensor was employed to measure the thrust force. The description and specifications of the measuring setup can be referred to Fig. S10(A) and Fig. S10(B). The measurement was repeated ten times with input currents ranging from 0.2 A to 0.6 A with increments of 0.05 A. The resulting average impact forces and their corresponding standard deviations for robots with coil set wide of 3 mm, 5 mm, and 8 mm are illustrated in Fig. 3A. The experimental results indicate that the MiaBot with a coil set wide of 5 mm exhibits the strongest impact among the different configurations. At an input current of 0.2 A, the average impact force measures 8.42 N, which increases to 16.67 N when the input current reaches 0.6 A. Although the impact force is slightly lower when coil set wides are 3 mm and 8 mm, it remains consistently above 13 N. Fig. 3B showcases the repeatability of the impacting behaviours of MiaBot, where the forward actuation current (I_l) is set between 0.2 A and 0.6 A, while the backward current (I_s) remains constant at 0.05 A. The actuation frequency is set at 2 Hz for one minute to evaluate the impact performance. The variance in impact force measurements is attributed to the ultra-short impact duration (typically less than 1 ms) between rigid bodies (magnet and robot stopper), which may introduce measurement errors in the force sensor.

The force of inertial impact is also affected by the material of the end cover. We compare the impact force using end covers made of different materials, including silicon, plastic, and metal (Shown in Fig. S10(C)). The results show that the robot with a silicon cover can significantly reduce the impact force because most

energy can be absorbed by the silicon cover. The aluminium end cover delivers the highest impact force, and the PLA cover is slightly inferior to the aluminium cover. Finally, the 3-D printed PLA cover is utilized as the stopper because of its convenience and cost-effectiveness in fabricating. We then tested its reliability and durability by up to 10,000 impacts (Fig. S10(D)). No significant changes in the permanent magnet's magnetic properties or physical appearance were observed after 10,000 impacts with an input current of 0.5 A, indicating the magnet can maintain a high and stable thrust force output under prolonged usage.

The high impact force of the design empowers MiaBot with a strong loading capability. Firstly, we investigated the locomotion performance of the robot with a load of 500 g (85.91 times its body weight). The quantitative investigation was conducted by applying a square wave signal with frequencies ranging from 1 Hz to 35 Hz, along with an I_l of 0.5 A. As shown in Fig. 3C, the optimal actuation frequency is dependent on the magnitude of the input current. Overall, the velocity increases with the applied frequency during the initial stage (below 10 Hz) because more impacting and locomotion cycles occur in a fixed period. As the frequency increases, a decline in the velocity occurs due to the frequent backward impacting process, which plays a role in cancelling the forward motion. In the third stage, the velocity rises again as the applied frequency increases because the inner magnet does not have sufficient time to contact and impact the back stopper, thus preventing the cancellation of the robot's forward motion. However, this upward trend is confined by an upper limit that can restrict the forward acceleration distance, resulting in reduced impact velocity and final impact force output. Detailed analysis and optimal selection of the input frequency can be found in Fig. S11. As shown in Fig. S11, we repeated experiments using I_l ranging from 0.3 A to 0.6 A. The four stages of frequency response are observed in all tested currents, and the most favourable choices of the driving currents converge around 25 Hz. Therefore, the optimized 25 Hz is set as the input frequency in the following experiments unless otherwise stated.

The locomotion performance with high loading capacity was subsequently assessed on a polymethyl methacrylate plate with the actuation frequency at the optimized frequency, i.e., 25 Hz (Fig. 3D). The results reveal a decrease in moving speed as the load increases from 100 g to 1000 g. With a load of 100 g, the millirobot achieves an average velocity of 618.74 mm/min. The speed decreases to 67.3 mm/min when the

payload increases to 1000 g (171.82 times its body weight). We calculate energy loss as the input energy minus the load kinetic energy, defining the loss rate as this deficit relative to the input energy. The results in Fig. 3D show the loss rate increases under heavier loads due to the enhanced robot-ground contact, which creates additional friction and results in greater frictional loss.

To investigate the robot's locomotion capability on different surfaces, we tested the MiaBot carrying 250 g of cargo on various surfaces. Fig. 3E demonstrates the locomotion speed of MiaBot on various sandpapers, with insets showing physical images (5x magnification) of four different roughness levels (i.e., 180 mesh, 400 mesh, 800 mesh, and 1000 mesh). The results show MiaBot maintains high payload capacity on rough surfaces whereas faster locomotion occurs on smoother surfaces. Additionally, we observed that velocity variance increases with surface roughness, which was attributed to irregular particulate protrusions that induce unstable friction forces on robot. Furthermore, to assess the locomotion reliability, the millirobot with a 500 g payload is tested on various surfaces such as metal, plastic, fabric, and wood (Fig. 3F, Video 1). The results prove that the millirobot is capable of carrying a heavy payload to move at a speed constantly above 110 mm/min on variety rigid surfaces. The mean cost of transportation is 178.1 (detailed data and definition is shown in Fig. S9(C)), which is relatively low for miniature robots of the comparable weight [32][46]. We observed that MiaBot's load-bearing capacity significantly decreases on flexible surfaces due to energy absorption by surface deformation and increased adhesion. As indicated by the small error bar in Fig. 3F, the locomotion is stable across most substrates, particularly on smooth surfaces that are not adhesive, such as fabric, wood, Teflon, and polyethylene. The snapshots of the robot moving on different surfaces are shown in Fig. S12.

Locomotion steerability

Bi-directional control is a highly desirable feature for miniaturized robots to complete point-to-point transportation tasks or navigate in confined environments (e.g., biological tubular organs or pipelines). In this study, the bi-directional control of the millirobot can be achieved by simply reversing the biased direction of the input signal (i.e., square wave). The snapshots in Fig. 4A(i) reveal that the MiaBot can

move back to the initial position after one minute of forward and then one minute of backward locomotion. The experiments were conducted using different bias currents and repeated ten times. Fig. 4A(ii) shows the real-time displacement of the MiaBot. The results show that the MiaBot can return to its initial position under various current inputs. The distance between the final positions and the starting points is less than 5mm, demonstrating that the MiaBot exhibits simple but high-precision directional control capabilities.

Maintaining a straight trajectory with heavy cargo by a single actuator-based robot is challenging, as misaligning the center of mass can create unwanted torque to disrupt locomotion. Full directional maneuverability is also essential for millirobots to perform complex tasks, such as trajectory following and navigating unstructured environments. In this study, the full-orientation adjustment is achieved by assembling two individual actuation units in parallel, and each of them can be controlled independently. The control system of the parallel units is illustrated in Fig. S13. To evaluate MiaBot's directional maneuverability, we compared two strategies in Fig. 4B. Fig. 4B(i) shows the conventional turning strategy commonly adopted by those actuators without bi-directional control capability. We can also use this method by activating one of the actuators. In this way, the turning radius can be adjusted by varying the input frequency and current of the active actuator. In contrast, Fig. 4B(ii) demonstrates MiaBot's ability to perform in-place turning by simultaneously controlling both actuators with opposite input signals, which allows the MiaBot to be deployed in more confined spaces.

To quantitatively evaluate the maneuverability, the millirobot was tested to turn 180^o on a polyvinyl chloride plate carrying payloads of 70 grams (Fig. 4C) and 500 grams of payload (Supplementary Movie 2). In Fig. 4C(i), we compare the time-cost for turning under two strategies: conventional single-side actuation and the proposed synergy actuation. Experimental results show that the in-place turning mode achieves approximately 1.5 times higher turning efficiency than the conventional mode. Fig. 4(ii) evaluates the drift of the robot's center during the 180^o turn. The input current (I_l) is kept at the same level of 0.5 A. Under conventional mode, the robot exhibits a significant drift of 361.12 mm, whereas synergy actuation reduces this drift to just 9.44 mm. The highly efficient, low-drift turning capability enabled by the proposed in-place turning control is useful for delivering heavy cargo in confined spaces.

To evaluate the trajectory-following capability, we conduct experiments by controlling the millirobot to follow a Z-shaped trajectory, including horizontal, vertical, left-turn, and right-turn tracks, using an open loop control scheme. The input current for the left and right actuators is illustrated in Fig. 4D(i). Initially, both actuators are operated with positive bias currents to move horizontally. As the robot approaches the left turn corner, the bias current of the left actuator is switched to a negative direction. In the subsequent vertical locomotion stage, both actuators' bias currents return to positive. During the right-turning process, the bias current of the right actuator is switched to the negative direction. Finally, the robot completes another horizontal locomotion stage using the same input current as the first stage. The process of the robot moving following the Z-shaped trajectory is shown in Fig. 4D(ii) and Supplementary Movie 3.

Locomotion in high frictional terrains

In this section, we present a series of experiments to demonstrate the MiaBot's locomotion capability on various terrains to overcome the high friction force. The demonstrated challenging tasks include transportation of heavy cargoes (Fig. 5A, Supplementary Movie 4), locomotion in viscous liquid (Fig. 5B, Supplementary Movie 5), operation in granular mediums (Fig. 5C, Fig. 5D, Supplementary Movie 6, Supplementary Movie 7), and drilling out through natural sand from a depth exceeding 100 mm (Supplementary Movie 8).

To optimize the performance of MiaBot in a liquid environment, slanted fins pointing backward were integrated into the millirobot to increase drag force and improve locomotion efficiency. In contrast, a smooth surface was designed on MiaBot to minimize friction when traversing within granular media. Additionally, all the tested millirobots were equipped with conical heads to reduce resistance drag force between the robot and the surrounding media.

Fig. 5A shows that the MiaBot is capable of carrying an 1800 g (309.28 times the robot's body weight) payload on a wooden surface. To the best of our knowledge, this work achieves a load-to-weight ratio exceeding 300 for a miniature robot, a performance that has not been previously reported. Theoretically, MiaBot could achieve a higher load-to-weight ratio as the impact force is higher than the static friction

force between MiaBot and the ground (Fig. S14). We only test 1800 g here as a proof of concept to verify the capability of navigating in a high-friction environment. As a universal design for high-friction environments, the MiaBot was also tested in a tank containing high-viscosity silicone oil (1000 cSt) (Fig. 5B). Despite the intermittent backward tendencies during the oscillating impact process, the presence of slanted fins effectively counteracts any backward movement owing to their greater resistance in the backward direction. The optimization design of slanted fins was proved through simulation and the steerability of MiaBot is demonstrated with the assistant of external magnetic field (Fig. S15). The findings suggest that the MiaBot holds the potential for applications in viscous environments (e.g., in crude oil pipelines). The MiaBot was also tested to traverse within a granular medium such as ceramic particles (diameter: 0.5 mm - 1.0 mm), as shown in Fig. 5C. A red flag was attached to the robot for demonstration purposes. Eventually, the robot emerged from the medium owing to the asymmetric resistance between its bottom and top surrounding environment (17). To simulate a natural environment, the robot was then tested underground amidst soil, sand, ceramic particles, and plants, as depicted in Fig. 5D. The results demonstrate the capability to navigate through various complex environments. Furthermore, the MiaBot's climbing performance was evaluated under high-friction conditions, including ascending steep 10° inclines and traversing gravel-filled environments with depths exceeding 100 mm (Fig. S16 and Supplementary Movie 8).

Potential applications of MiaBot in flexible tube inspection

Regular inspection and maintenance of small-diameter pipelines in high-end equipment, particularly for detecting internal blockages and cracks, are critical to operational efficiency and safety. However, traditional endoscopic probes cannot navigate deep tortuous segments, whereas the proposed MiaBot demonstrate high efficacy in traversing these constrained environments despite gravitational loads and wall pressures. As illustrated in Fig. 6A, small robots face significant challenges in overcoming high-friction environments when the flexible tube walls press against them. For the proposed MiaBot, the internal magnet achieves a speed of 2.93 m/s under the influence of the inner actuation force generated by a 0.5 A input

current. The instantaneous propulsion force resulting from collisions enables the MiaBot to overcome frictional resistance, facilitating its locomotion within flexible tubular environments. Vertical and three-dimensional tubular navigation poses significant challenges for millirobots, as their limited actuation force often fails to overcome the resistance from high friction and gravitational effects. This typically results in downward sliding and insufficient upward mobility. However, the spatially distributed complex tubing systems are widely employed in high-end equipment for gas-liquid transportation. To enable the deployment in such environments, we implemented the MiaBot with a resistance regulation strategy in the flexible tubes. The system's strong instantaneous propulsion enables MiaBot to achieve rapid motion against both gravity and pipeline friction. In the experiment, MiaBot successfully navigated through a 60 cm vertical pipeline in 60 s with a 10 Hz square wave driving signal at +0.5 A forward and -0.05 A reverse (see Fig. 6B, Supplementary Movie 9). For equivalent-length three-dimensional spatial navigation, the robot required approximately 100 s (Fig. 6C), with this delay attributed to high frontal resistance from the narrow inner surface of the silicone tube. In addition, Fig. 6D and Supplementary Movie 10 present process of the MiaBot navigating through a narrow silicone tube environment with an integrated camera. Experimental results demonstrate that the MiaBot successfully traverses a 680 mm silicone tube with straight and curved trajectories in under 200 seconds. Insets in Fig. 6D highlight the narrow and deformable nature of the silicone tube, which tightly envelopes the robot. With the compact camera, the MiaBot has the potential for applications in pipeline inspection. Fig. 6E illustrates the inspection process, with the top images (Fig. 6E(i)) showing the MiaBot’s position via external views, while the bottom photos (Fig. 6E(ii)) display corresponding inspection results captured by the onboard camera. Moreover, the robot's real-time position can be tracked using a magnetic tracking system (Fig. S16), demonstrating the potential of closed-loop control for precise navigation. This is particularly useful for performing tasks at designated locations in tubular environments without external line of sight. The demonstration indicates that MiaBot has the potential to detect and location the defects in industrial pipeline systems.

Discussion

In this study, we developed a millirobot using the robot's inner magnetic interaction force as the actuation force. The proposed actuation method, based on local magnetic forces and the momentum conservation principle, offers several significant benefits. First, the straightforward energy conversion mechanism of the proposed MiaBot allows it a direct, powerful force output at a smaller scale than conventional electromagnetic motors that output torque and rely on complicated gears and bearing systems. Second, the momentum conservation-based impact motion enables the MiaBot to have a strong instantaneous propulsion force, allowing it to be deployed in various high-frictional environments. Third, the robot is not restricted to a limited workspace, as the inner actuation mechanism can propel the robot regardless of the millirobot's position and get a higher actuation force with lower power consumption due to the close distance between the coils and the inner magnet. To achieve maximum impact force and efficiency, we theoretically modelled the magnetic interaction force and impact energy and optimized the design of the robot frame. These design considerations enable the MiaBot to deliver large force output while maintaining the robot at a small scale.

The distinguished loading performance in this study demonstrates the capability to overcome the high friction on the ground. We provide a comprehensive comparison of the load-carrying capacity of MiaBot with various state-of-the-art small robots that utilize different actuation mechanisms, including shape memory alloy, dielectric elastomer actuators, piezoelectric motors, magnetic polymers, and thermally sensitive materials (Fig. 1D and Table S2). The results show that the majority of existing small robots are capable of transporting cargo weighing less than 50 times their own weight. Only two studies report load capacities exceeding 100 times body weight, but their miniature size (<0.05 g) restricts absolute payloads to <5 g. The SMA-, DEA-, and PZT-driven robots, which share comparable scales and similar wired actuation systems with our design, exhibit the load-to-weight ratios below 30. In contrast, the proposed MiaBot achieves a payload of 1800 g, corresponding to a load ratio of 309.28. Additionally, we compared the loading capabilities of the proposed robot and various creatures, such as ants, beetles, eagles, chimpanzees, human beings, and elephants (Fig. 1D and Table S3). The results highlight the MiaBot's

loading capability compared to most mammals, which typically carry cargo less than ten times their own weight. The proposed new millirobot outperforms most of the ant species. While beetles are renowned for their impressive load-bearing capacity, the MiaBot demonstrates a comparable capability. These findings underscore the exceptional load-carrying potential of MiaBot, solidifying its position as a leading contender in millirobotics.

The MiaBot also demonstrates locomotion capabilities, particularly in challenging environments characterized by high friction, such as silicone oil with a viscosity of 1000 cSt (Fig. 5B), granular media (Fig. 5C, Fig. 5D), and deep natural sand. These experiments highlight the potential of MiaBot for various applications in industrial and agricultural domains. For instance, MiaBot can be equipped with a vision inspection unit to detect defects in oil pipelines. Furthermore, pH and moisture sensors can be integrated into MiaBot to monitor the physicochemical properties of soil. Another advantage of MiaBot lies in its precise steerability and controllability. Bidirectional control is achieved simply by reversing the bias current direction. Furthermore, the proposed full directional control strategy demonstrates enhanced turning efficiency and a reduced turning radius compared to conventional single-actuator methods (Fig. 4). Additionally, we demonstrated MiaBot's motion capability in flexible pipelines that are curved, vertical, and narrower than its own diameter. With an integrated camera system, MiaBot can effectively inspected pipeline interiors (Fig. 5).

While MiaBot shows promising potential, further refinements could broaden its applicability. Currently, the coil surface increases by approximately 50°C after operating for 300 seconds. Although this temperature is acceptable for the robot, prolonged operation risks thermal damage. Addressing this requires an optimized design to eliminate direct coil-skin contact and integrate liquid cooling, which would enhance heat dissipation and ensure long-term safety. Additionally, noise generated by the inner magnet’s periodic impacts could be reduced by encasing the robot in a soundproof enclosure or applying sound-absorbing materials to its surface. The applicability of MiaBot could be further expanded with onboard power solutions, as the maximum operating voltage in this study is below 6 V, with a current of 0.5 A. Future

work will involve implementing lithium battery power and developing onboard circuits with Bluetooth communication for remote control. This will enable remote switching of embedded H-bridge circuits to generate the necessary square wave signals for actuating the robot. On the other hand, although MiaBot has shown great performance in high-resistance environments, it can be further improved in specific environment. For instance, in liquid environments, optimization of the robot's fin angle and scale could improve its propulsion efficiency. In pipe environments, adding wheel structures and variable diameter mechanisms could enhance adaptability. Additionally, reducing the robot's size could open up potential applications in human organs, such as the gastrointestinal tract or cardiovascular system.

In summary, this study presents the design of an inner actuated millirobot, namely MiaBot, which utilizes local magnetic forces for actuation and inertial impact to enhance output force. The MiaBot achieves a thrust force of 15.02 N under a 0.5 A current input, a performance that significantly surpasses most comparable systems, which typically produce forces below the Newton scale. Leveraging its substantial output force, the MiaBot demonstrates impressive capabilities, including transporting cargo exceeding 309 times its body weight, navigating through high-viscosity environments, and traversing deep granular media. These features position the MiaBot as a valuable tool for navigating harsh environments, such as oil pipelines or underground sand. Furthermore, its maneuverability, characterized by high turning efficiency and a small turning radius (with theoretically zero drift of the center of mass), makes it well-suited for deployment in confined spaces. The MiaBot also exhibits fast locomotion in pipelines, with speeds reaching up to 113.66 mm/s, showcasing its potential for completing tasks in tubular environments. Overall, the MiaBot represents a significant advancement in millirobotics, with promising potential to address complex challenges in high-friction and constrained spaces.

Methods

Materials for fabricating the MiaBot

Magnet: The permanent magnet used in MiaBot is made of NdFeB, Grade N52 (K&J Magnetics, Inc., USA). The cylindrical magnet is used in this paper with an overall dimension of 6.35 mm in diameter and

6.35 mm in thickness. The surface field of the magnet is 6619 Gauss. The calibration process of the magnetic moment is available in supplementary materials (Fig. S2). The skeleton used for housing the permanent magnet and mounting the electromagnetic coil is Polyetheretherketone (PEEK), which is machined with a center channel of 6.5 mm for passing through the magnet. The PEEK has the properties of a smooth surface and high-temperature resistance (2600 for long-time operating). Two end covers are printed by a commercial FDM printer (Method, MakerBot Inc., USA). The filament is made of Polylactic acid (precision material, Method series). And the printed layer thickness layer is 0.06 mm. The end cover is firmly attached to the frame using super glue (Loctite® 406). The wire for forming the electromagnetic coil is an enamel-insulated wire with a diameter of 0.15 mm. The copper wire has the properties of good conductivity and flexibility (Baoling Jiang Shu, China).

Signal-generating and validation

A three-channel wave generator is used to generate the desired signal (FY8300, FeelElec Inc., China). The three channels can provide any waveforms according to the generating commands and can be independently controlled. The controllable parameters include frequency, duty cycle, bias voltage, etc. The generated wave is then amplified to a suitable voltage via an amplifier with a limited voltage of 50 V and a current of 4 A (PS-LG504, Hu Nan Pai Sheng Elegance Technology CO., LTD). On the one hand, the output voltage is connected to the MiaBot to drive the robot. On the other hand, the real-time current is also monitored by an oscilloscope (TBS 1102C, Tektronix) to determine whether the waveform meets the driving requirements.

Acceleration time of the permanent magnet

The acceleration time of the permanent magnet from one end of the center channel to the other is reflected by a high-speed camera (pco. dimax S4, PCO.). The high-speed camera can record videos at 4500fps with 1008×1008 pixels.

Impact force measurement

A piezoelectric force sensor is applied to measure the impact force of the permanent magnet (1051V1, DYTRAN, USA). The sensor can measure the force up to 10Lb with a frequency of 50 kHz. The measured signals are then stored in a data acquisition system (IOLITEi-1xACC, Althen sensors & controls)

Position and speed measurement

The real-time state of the MiaBot is captured by a CMOS camera (JW-02, tiantianquan). The figures are then transferred to the host computer and processed by MATLAB (MathWorks. Inc) for real-time position and orientation detection.

Thermal and magnetic field measurement

The temperature of the electromagnet is measured by an infrared thermal imager (UTi260B, UNI-T). The magnetic field density is detected by a Gaussmeter (HGM09s from MAGSYS) with a measuring range from 1 mT to 4.5T and a resolution of 1 μ T.

Experimental adaptability of the MiaBot

The silicon oil used for evaluating the experimental adaptability of the MiaBot is PX-200 (DOW CORNING). The granular medium used here is hollow ceramic microbeads with a diameter of 20-40 mesh (Henan Hengyuan New Material Co., Ltd). The natural sand is from the Tengger Desert (Gan Su province).

Data Availability

The original experimental data generated in this study have been deposited in the Figshare database under accession code: 10.6084/m9.figshare.30598439

References

1. Gu GY, Zou J, Zhao RK, Zhao XH, Zhu XY. Soft wall-climbing robots. *Science Robotics* **3**, (2018).

2. Pang WB, *et al.* A soft microrobot with highly deformable 3D actuators for climbing and transitioning complex surfaces. *Proceedings of the National Academy of Sciences of the United States of America* **119**, (2022).

3. Hong S, Um Y, Park J, Park HW. Agile and versatile climbing on ferromagnetic surfaces with a quadrupedal robot. *Science Robotics* **7**, (2022).

4. Tang C, *et al.* A pipeline inspection robot for navigating tubular environments in the sub-centimeter scale. *Science Robotics* **7**, (2022).

5. Ze QJ, *et al.* Soft robotic origami crawler. *Science Advances* **8**, (2022).

6. Zhang JC, *et al.* Voxelated three-dimensional miniature magnetic soft machines via multimaterial heterogeneous assembly. *Science Robotics* **6**, (2021).

7. Li GR, *et al.* Self-powered soft robot in the Mariana Trench. *Nature* **591**, 66 (2021).

8. Al Khatib E, Bhattacharjee A, Razzaghi P, Rogowski LW, Kim MJ, Hurmuzlu Y. Magnetically actuated simple millirobots for complex navigation and modular assembly. *IEEE Robotics and Automation Letters* **5**, 2958-2965 (2020).

9. Rogowski LW, Bhattacharjee A, Zhang X, Kararsiz G, Fu HC, Kim MJ. Magnetically programmable cuboids for 2D locomotion and collaborative assembly. In: *2020 IEEE/RSJ International Conference on Intelligent Robots and Systems (IROS)*). IEEE (2020).

10. Erin O, *et al.* Overcoming the Force Limitations of Magnetic Robotic Surgery: Magnetic Pulse Actuated Collisions for Tissue-Penetrating-Needle for Tetherless Interventions. *Advanced Intelligent Systems* **4**, (2022).

11. Li M, Pal A, Aghakhani A, Pena-Francesch A, Sitti M. Soft actuators for real-world applications. *Nature Reviews Materials* **7**, 235-249 (2022).

12. Hines L, Petersen K, Lum GZ, Sitti M. Soft Actuators for Small-Scale Robotics. *Advanced Materials* **29**, (2017).

13. Kellaris N, Venkata VG, Smith GM, Mitchell SK, Keplinger C. Peano-HASEL actuators: Muscle-mimetic, electrohydraulic transducers that linearly contract on activation. *Science Robotics* **3**, (2018).

14. De Pascali C, Naselli GA, Palagi S, Scharff RBN, Mazzolai B. 3D-printed biomimetic artificial muscles using soft actuators that contract and elongate. *Science Robotics* **7**, (2022).

15 Bhattacharjee A, Lu Y, Becker AT, Kim M. Magnetically controlled modular cubes with reconfigurable self-assembly and disassembly. *IEEE transactions on robotics* **38**, 1793-1805 (2021).

16. Elliot W. Hawkes DLC, and Mark R. Cutkosky. Vertical dry adhesive climbing with a 100× bodyweight payload. In: *2015 IEEE International Conference on Robotics and Automation (ICRA)*) (2015).

17. Lu HJ, *et al.* A bioinspired multilegged soft millirobot that functions in both dry and wet conditions. *Nature Communications* **9**, (2018).

18. Zhang L, Abbott JJ, Dong LX, Kratochvil BE, Bell D, Nelson BJ. Artificial bacterial flagella: Fabrication and magnetic control. *Applied Physics Letters* **94**, (2009).

19. Tang YC, Li MT, Wang TL, Dong XG, Hu WQ, Sitti MT. Wireless Miniature Magnetic Phase-Change Soft Actuators. *Advanced Materials* **34**, (2022).

20. Naclerio ND, *et al.* Controlling subterranean forces enables a fast, steerable, burrowing soft robot. *Science Robotics* **6**, (2021).

21. Leclerc J, Ramakrishnan A, Tsekos NV, Becker AT. Magnetic hammer actuation for tissue penetration using a millirobot. *IEEE Robotics and Automation Letters* 3, 403-410 (2017).

22. Xiang YX, *et al.* MINRob: A Large Force-Outputting Miniature Robot Based on a Triple-Magnet System. *Ieee Transactions on Robotics* **40**, 3127-3145 (2024).

23. Taddese AZ, Slawinski PR, Pirotta M, De Momi E, Obstein KL, Valdastri P. Enhanced real-time pose estimation for closed-loop robotic manipulation of magnetically actuated capsule endoscopes. *International Journal of Robotics Research* **37**, 890-911 (2018).

24. Liang C, Wang YQ, Yao T, Zhu BT. A shape memory alloy-actuated soft crawling robot based on adaptive differential friction and enhanced antagonistic configuration. *Journal of Intelligent Material Systems and Structures* **31**, 1920-1934 (2020).

25. Lin HT, Leisk GG, Trimmer B. GoQBot: a caterpillar-inspired soft-bodied rolling robot. *Bioinspiration & Biomimetics* **6**, (2011).

26. Huang WQ, Shang WF, Huang YH, Long HY, Wu XY. Insect-Scale SMAW-Based Soft Robot With Crawling, Jumping, and Loading Locomotion. *Ieee Robotics and Automation Letters* **7**, 9287-9293 (2022).

27. Liu HQ, Yang C, Xu ZY, Lv M, Zhou RG. Improvement of Adaptive Motion Performance in a Flexible Actuator, Based on Electrically Induced Deformation. *Actuators* **11**, (2022).

28. Wu C, Yan H, Cai AJ, Cao CJ. A Dielectric Elastomer Actuator-Driven Vibro-Impact Crawling Robot. *Micromachines* **13**, (2022).

29. Sun YH, *et al.* Origami-inspired folding assembly of dielectric elastomers for programmable soft robots. *Microsystems & Nanoengineering* **8**, (2022).

30. Li QZ, Zhang FK, Jing ZY, Yu FJ, Chen Y. A Hybrid Territorial Aquatic Bionic Soft Robot with Controllable Transition Capability. *Journal of Bionic Engineering* **20**, 568-583 (2023).

31. Ceponis A, Mazeika D, Jurenas V, Deltuviene D, Bareikis R. Ring-Shaped Piezoelectric 5-DOF Robot for Angular-Planar Motion. *Micromachines* **13**, (2022).

32. Miao ZC, *et al.* Power Autonomy and Agility Control of an Untethered Insect-Scale Soft Robot. *Soft Robotics* **10**, 749-759 (2023).

33. Ji XB, *et al.* An autonomous untethered fast soft robotic insect driven by low-voltage dielectric elastomer actuators. *Science Robotics* **4**, (2019).

34. Hernando-García J, García-Caraballo JL, Ruiz-Díez V, Sánchez-Rojas JL. Comparative Study of Traveling and Standing Wave-Based Locomotion of Legged Bidirectional Miniature Piezoelectric Robots. *Micromachines* **12**, (2021).

35. Joyee EB, Pan YY. A Fully Three-Dimensional Printed Inchworm-Inspired Soft Robot with Magnetic Actuation. *Soft Robotics* **6**, 333-345 (2019).

36. Hua DZ, Liu XH, Sun SS, Sotelo MA, Li ZX, Li WH. A Magnetorheological Fluid-Filled Soft Crawling Robot With Magnetic Actuation. *Ieee-Asme Transactions on Mechatronics* **25**, 2700-2710 (2020).

37. Yin XC, Yan JC, Wen S, Zhang JT. Magnetorheological Fluid-Filled Origami Joints With Variable Stiffness Characteristics. *Ieee-Asme Transactions on Mechatronics* **28**, 1546-1557 (2023).

38. Wang Q, Lu XL, Yuan NY, Ding JN. Small-Scale Soft Robot with High Speed and Load Capacity Inspired by Kangaroo Hopping. *Advanced Intelligent Systems* **4**, (2022).

39. Huang H, Feng Y, Yang X, Yang L, Shen YJ. An Insect-Inspired Terrains-Adaptive Soft Millirobot with Multimodal Locomotion and Transportation Capability. *Micromachines* **13**, (2022).

40. Yang RL, Zhu YJ, Chen FF, Qin DD, Xiong ZC. Superhydrophobic Photothermal Paper Based on Ultralong Hydroxyapatite Nanowires for Controllable Light-Driven Self-Propelled Motion. *Acs Sustainable Chemistry & Engineering* **7**, 13226-13235 (2019).

41. Zhao Y, Hong YY, Qi FJ, Chi YD, Su H, Yin J. Self-Sustained Snapping Drives Autonomous Dancing and Motion in Free-Standing Wavy Rings. *Advanced Materials* **35**, (2023).

42. Liang RX, Yu HJ, Wang L, Shen D. Light-Guided Dynamic Liquid Crystalline Elastomer Actuators enabled by Mussel Adhesive Protein Chemistry. *Advanced Functional Materials* **33**, (2023).

43. Ma Y, Zhang YY, Wu BS, Sun WP, Li ZG, Sun JQ. Polyelectrolyte Multilayer Films for Building Energetic Walking Devices. *Angewandte Chemie-International Edition* **50**, 6254-6257 (2011).

44. Zhang YF, Zhu RJ, Wu JH, Wang HQ. SimoBot: An Underactuated Miniature Robot Driven by a Single robot. IEEE/ASME Transactions on Mechatronics **27**, 5748-5759 (2022).

Acknowledgements

This work is financially supported by the Research Grant Council (RGC) of Hong Kong under Grant 11212321, 11217922, and 21212720; and in part by the Science, Technology and Innovation Committee of Shenzhen under Grant SGDX20210823104001011, and the Start-up Research Fund of Central South University under Project No. 502044037

Author Contributions

M.W. and J.L. conceived and designed the study. W.W. and Z.Z. assisted with robot fabrication and figure preparation. M.W. and J.L. conducted the experiments and analyzed the data. M.W., Y.X., and J.Z. developed the kinematic modeling. W.W., T.W., R.L., W.D., and S.W. assisted with the experiments and data analysis. M.W. wrote the manuscript with input from all authors. J.L. provided constant feedback and suggestions throughout all experiments. J.L., Z.W., and J.Z. supervised the study and edited the manuscript. All authors discussed the results and reviewed the manuscript.

Competing Interests

The authors declare no competing interests.

Figure legends

Fig. 1: Overview and locomotion mechanism of MiaBot. (A) An image of a MiaBot and an exploded view of the design. **(B)** Comparison of load-carrying capability between the proposed MiaBot with the existing millirobots less than 10 g. (SMA: Shape memory alloy, DEA: Dielectric elastomer actuators, PZT: Piezoelectric actuators). **(C)** The snapshot of one actuation cycle: MiaBot carrying 500 g load actuated by a biased square wave (0.5A and -0.05A) signal. **(D)** Position of the inner magnet and the corresponding force on the MiaBot during one actuation cycle. When the applied current is 0.5 A, the magnet accelerates from one end to the other within 20 ms and generate a theoretical impact force greater than 19 N. The magnet is repositioned to its initial position using a lower current (-0.05 A). **(E)** The schematic diagram shows that MiaBot is capable of exploring various terrains with high friction, such as granular medium, viscous liquids, and large payload transportation, due to the strong impact force.

Fig. 2: Locomotion modes and design optimization of MiaBot. (A) Two locomotion modes of MiaBot: (i) Without load, locomotion is dominated by the attraction force between the magnet and coils, moving the robot opposite to the magnet. (ii) With a heavy load, locomotion is dominated by the inertial impact force between the magnet and the stopper, causing the robot to move in the same direction as the magnet. **(B)** Experimental analysis of the relationship between locomotion modes and load weight under various input currents. **(C)** Numerical simulation of the effect of channel length (L_c) and coil holder length (L_w) on the magnet's velocity before impacting. **(D)** Traveling time of the magnet decreases with increasing driving current, with optimal results achieved when L_w is 5 mm. **(E)** Validation of numerical simulations through experimental measurements of the magnet's final impact velocity. **(F)** Locomotion speed of bare MiaBot in an acrylic tube, driven by a square wave ranging from 0.5 A to -0.05 A. Error bars represent the standard deviation, based on ten independent experiments.

Fig. 3: Inertial impact force and loading performance of MiaBot. (A) Relationship between impact force and applied current for different widths of coil set (3 mm, 5 mm, and 8 mm). **(B)** Repeatability of impact force under various actuation currents. **(C)** Locomotion velocity versus excitation frequency with a 500 g load. **(D)** The locomotion velocity decreases with increased payload, while the energy loss ratio rises due to the higher friction induced by the added weight. **(E)** Locomotion velocity on sandpaper surfaces with varying grit sizes (180, 400, 800, and 1000). Insets: 5x magnified images of sandpaper textures. **(F)** Locomotion velocity on different surface materials. Error bar conventions, as described in Fig. 2.

Fig. 4: Steerability of MiaBot. (A) Bidirectional control: (i) Snapshots showing the MiaBot return to its initial position after 60 seconds of forward followed by 60 seconds of backward locomotion; (ii)

Displacement during 120 seconds of forward and backward movement. **(B)** Comparison of turning strategies: (i) Conventional turning with two actuators lacking bidirectional control; (ii) Proposed in-place turning using the synergistic operation of two actuators in opposite directions. **(C)** Comparison of two turning strategies: (i) Time efficiency demonstrates higher performance with the in-place turning strategy; (ii) The trajectory of the robot's center shows in-place turning maintains a stationary mass center. **(D)** Trajectory following: (i) Input signal for left and right actuators; (ii) Snapshots of the Z trajectory following. Error bar conventions, as described in Fig. 2.

Fig. 5: Demonstration of locomotion in high-friction terrains. (A) Snapshots of MiaBot carrying heavy cargo (1800 g, 309.28 times its weight) on solid ground. **(B)** Locomotion through high-viscosity media (silicone oil, 1000 cSt). **(C)** Locomotion under granular media (ceramic beads). **(D)** Steering in natural terrains, including soil, sand, and gravel.

Fig. 6: Inspection in a confined flexible tubular environment. (A) Schematic of MiaBot navigating a narrow, flexible silicone tube. **(B)** Locomotion in a vertical tube. (**C**) Locomotion through a tube in 3-D space. **(D)** Snapshots of MiaBot traversing straight and curved trajectories with an onboard camera. Inset: Diameter comparison of MiaBot and the silicone tube. **(E)** The external and internal view during tube inspection: External view showing the position of MiaBot within the tube; (ii) internal view captured by the camera showing the interior conditions of the tube.

Editor Summary:

The authors developed a 5.82 g magnetically inner-actuated millirobot capable of carrying over 300 times its own weight. The high thrust and payload capability enable it to navigate tough terrains, such as sand, viscous oil, and confined spaces.

Peer Review Information:

Nature Communications thanks Islam Khalil, Louis William Rogowski and the other anonymous, reviewer(s) for their contribution to the peer review of this work. A peer review file is available.

A

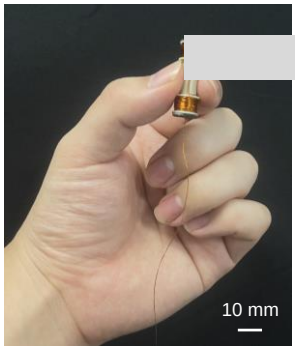

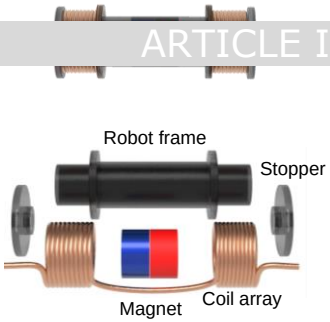

B

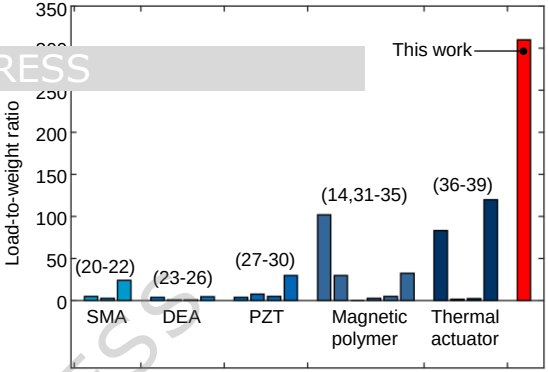

C

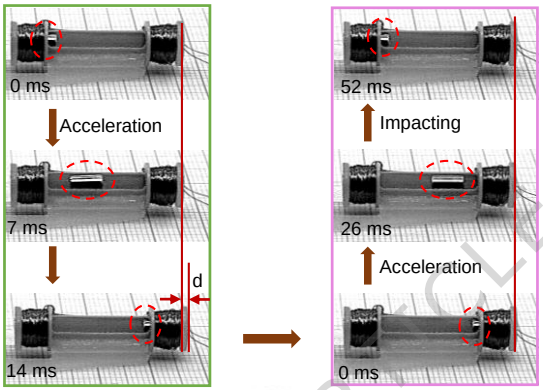

D

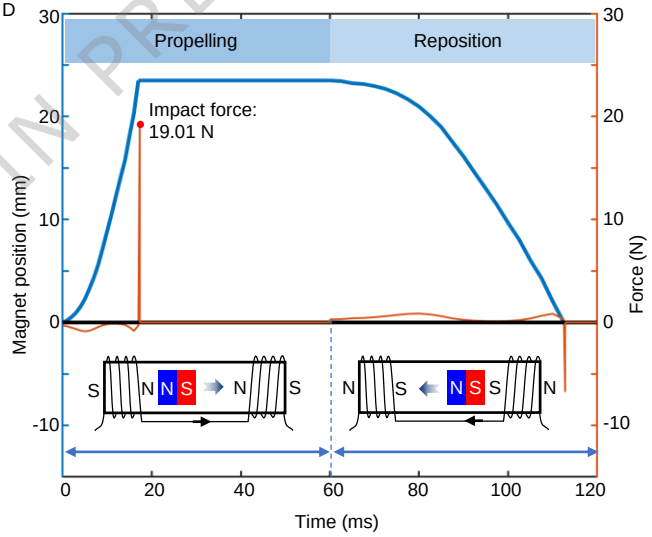

E

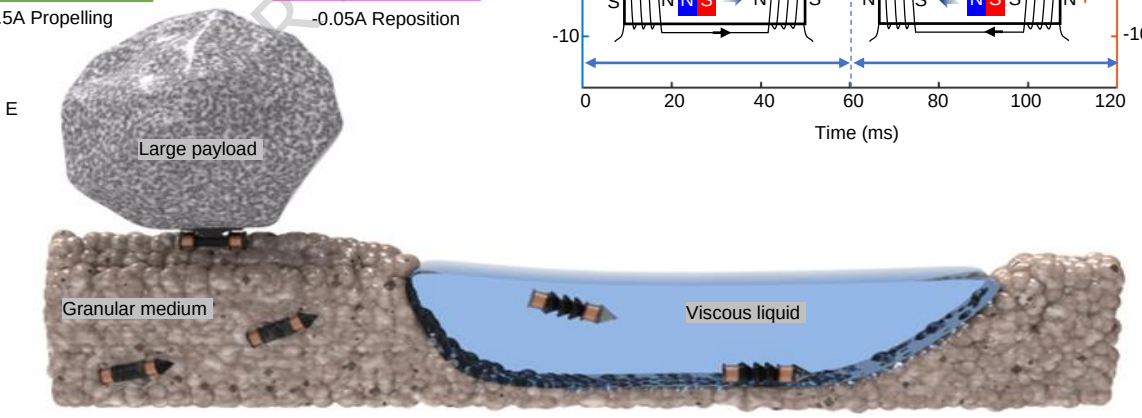

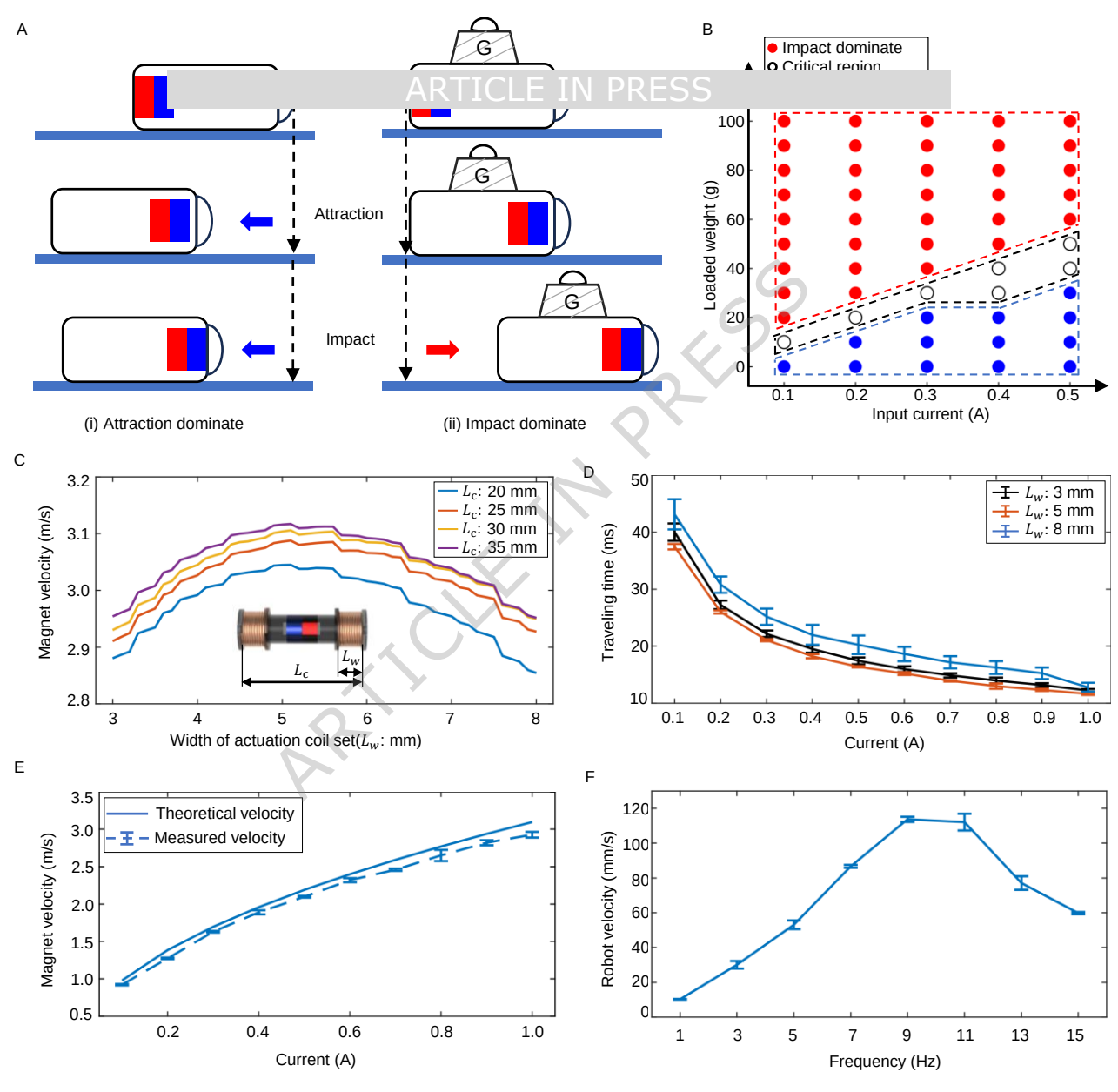

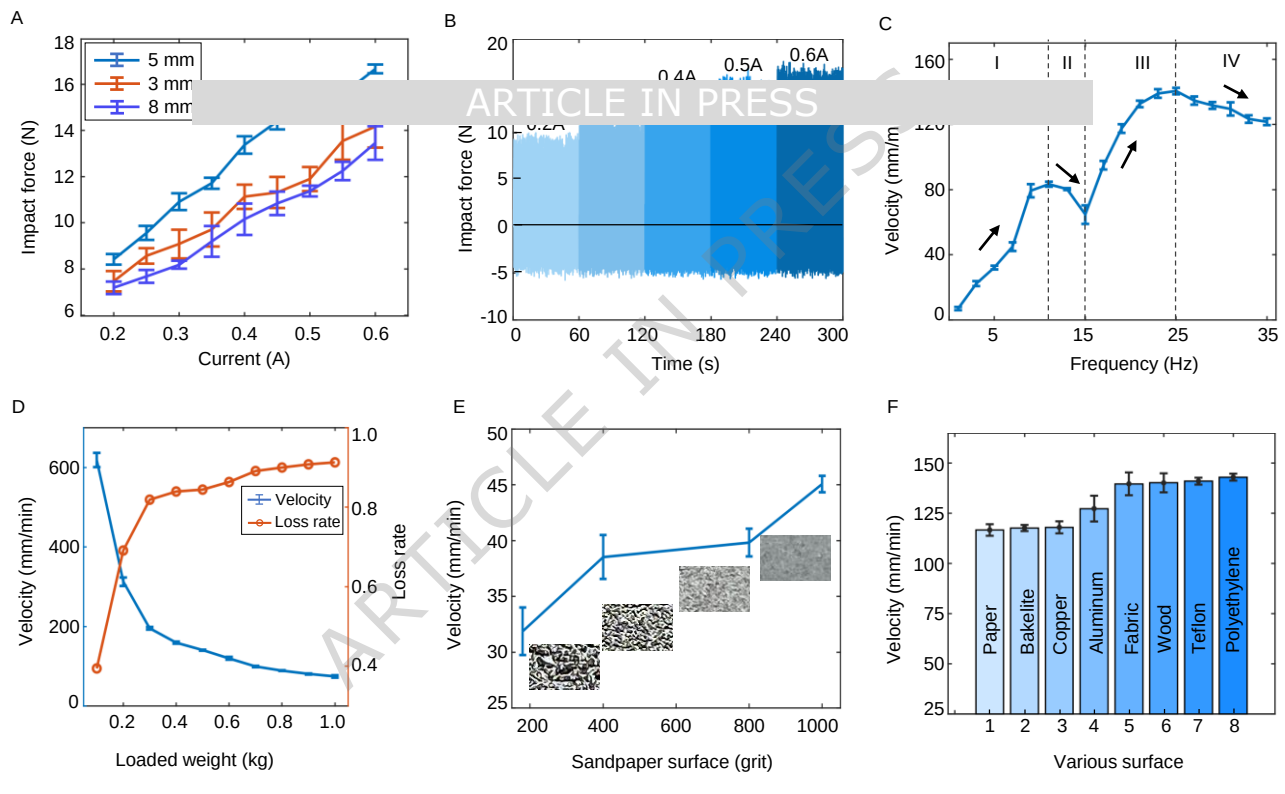

A

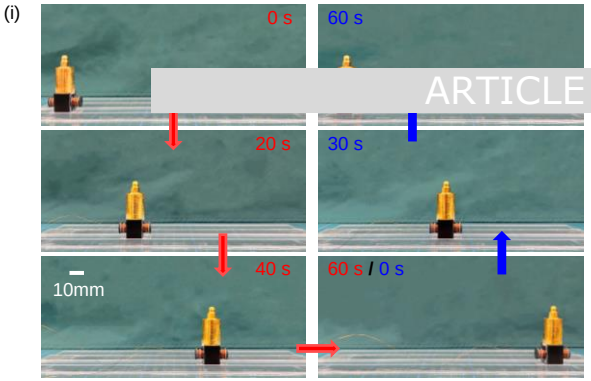

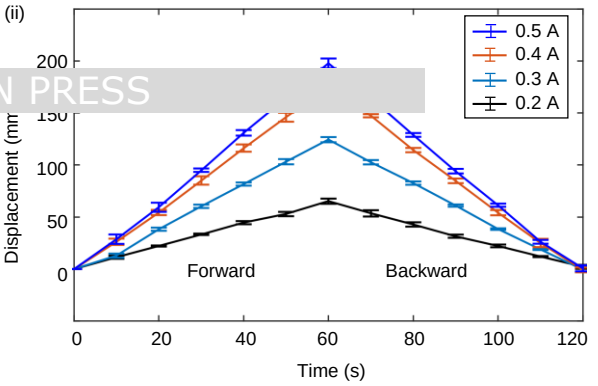

B

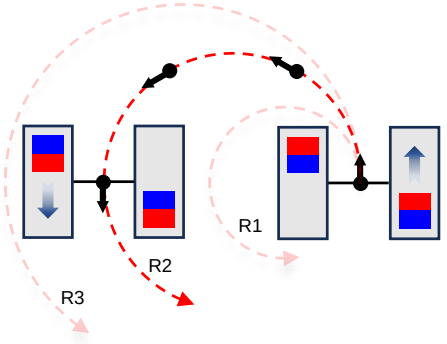

(i) Turning with controllable radius

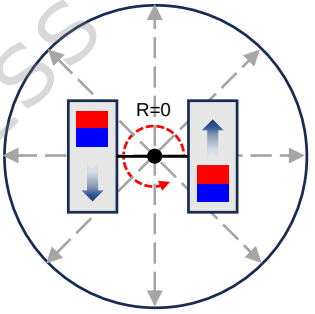

(ii) In-place turning strategy

C

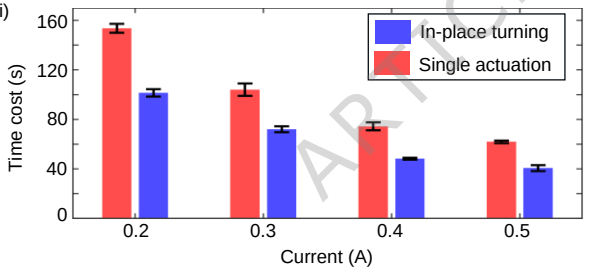

D

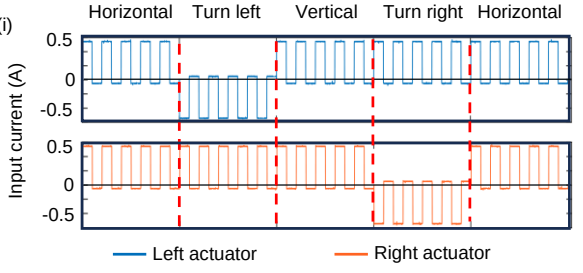

(ii)